Corrosion Science 110 (2016) 200–212

Contents lists available at ScienceDirect

Corrosion Science

journal homepage: www.elsevier.com/locate/corsci

Degradation of ferritic stainless steels under conditions used for solid oxide fuel cells and electrolyzers at varying oxygen pressures

P. Alnegren*, M. Sattari, J. Froitzheim, J-E. Svensson

Environmental Inorganic Chemistry, Chalmers University of Technology, Kemivägen 10, SE-41296 Gothenburg, Sweden

ARTICLE INFO

Article history:
Received 11 December 2015
Received in revised form 18 April 2016
Accepted 20 April 2016
Available online 21 April 2016

Keywords:
A. stainless steel
B. SEM
B. XRD
C. high temperature corrosion

ABSTRACT

Four commercial ferritic stainless steels were tested at 850 °C in oxygen pressures ranging from 10^{-4} to 1 atm, in order to investigate the isolated effect of oxygen pressure on corrosion, in the context of solid oxide electrolysis cells. The oxidation rates of all steels were essentially independent of oxygen partial pressure, which indicates n-type behavior. FIB/SEM analysis revealed that the grain size of the oxides was found to decrease at lower oxygen pressures. Volatile Cr species evaporation in pure oxygen was significantly lower than what has been reported for simulated solid oxide fuel cell environments with humid air.

1. Introduction

Solid oxide fuel cells (SOFCs) are able to convert chemical energy from fuels directly into electricity with high efficiency and without combustion. Due to the high operating temperature other fuels in addition to pure hydrogen, such as natural gas, can be used. This makes them suitable for applications such as combined heat and power units in households [1] and auxiliary power units in trucks [2], but they are also considered for power plant scale electricity production [3,4]. Moreover, SOFCs can run in reverse mode, i.e. to electrolyze steam into hydrogen by feeding water and electric current to produce hydrogen and oxygen, and are then referred to as solid oxide electrolysis cells (SOEC). The high operating temperature gives SOECs exceptionally high efficiencies and the ability to electrolyze carbon dioxide into carbon monoxide, which in combination with water electrolysis makes syngas production possible [5,6]. But a common challenge for both SOFC and SOEC technology is to increase operating lifetime with sufficiently low cost materials. The cost of material degradation have been pointed out as one of the main contributors to the hydrogen price for electrolyzed H_2 production [7].

In order to increase power density, individual cells are interlinked to form a stack of cells. Interconnects are components that provide electrical contact between adjacent cells and separate and distribute the fuel and oxidant gases [8,9]. In planar stacks, the interconnects make up a large part of the total material used and are thus a considerable cost [10]. The most commonly considered materials for interconnects are ferritic stainless steels due to their desirable properties, such as matching thermal expansion coeffient (TEC) with other cell components, ease of fabrication, high thermal and electrical conductivity and the formation of oxide products with an acceptably low electrical resistance, i.e. chromium oxide [11]. The buildup of oxide products, or corrosion, is one of the main material issues with metallic interconnects. Both anode and cathode environments in SOFC and SOEC stacks causes ferritic stainless steels to oxidize. During operation a Cr_2O_3 scale continuously grows on the substrate surface, resulting in a steady increase in electrical resistance [12–14]. Eventually, the increased oxide thickness will lead to spalling of the oxide scale and consequently lost electrical contact between electrodes and interconnects [15]. Another challenge with chromia-forming interconnects is to reduce chromium evaporation and the consequent poisoning of electrodes [16,17]. Several coating solutions have been developed that minimize chromium evaporation and slow down oxidation [13]. These include different spinel and perovskite cap layers as well as the addition of reactive elements such as yttrium, cerium or hafnium [13,18,19].

Studies that have investigated degradation in simulated fuel electrode and oxygen/air electrode environments have led to discrepancies in whether oxidation is slower, faster or unchanged [11,20]. The oxidation mechanisms in fuel and oxygen environments are often discussed in terms of oxygen partial pressure since the concentration of oxygen at the fuel electrode is several orders of magnitude lower than at the oxygen electrode. Palcut et al. studied ferritic stainless steels with chromium contents of 20–29% in dry

* Corresponding author.
E-mail addresses: alnegren@chalmers.se, patrik.alnegren@gmail.com (P. Alnegren).

http://dx.doi.org/10.1016/j.corsci.2016.04.030
0010-938X/

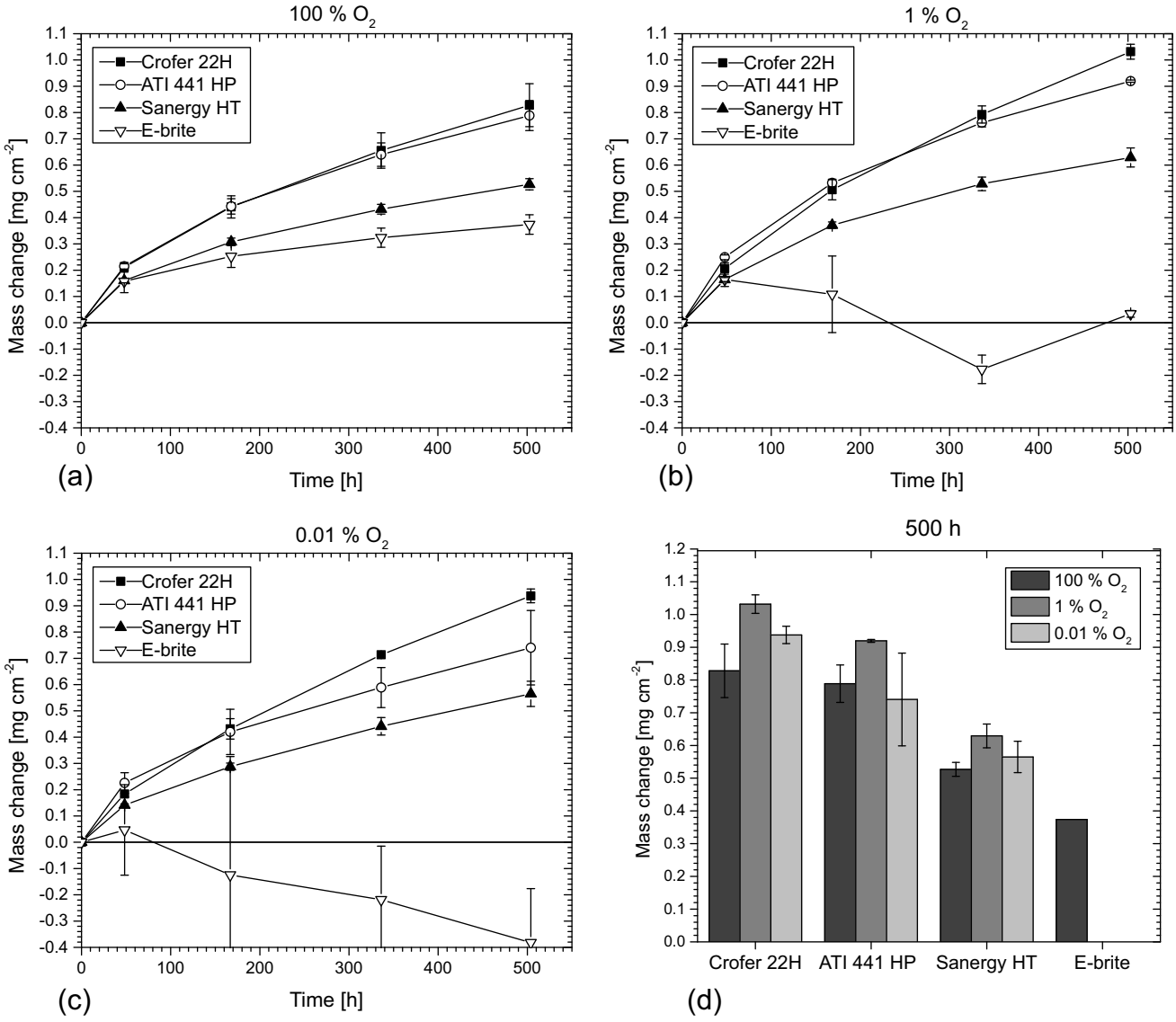

Fig. 1. Oxidation kinetics for Sanergy HT, Crofer 22 H, E-Brite and 441HP in (a) 100% O_2 (b) 1% O_2 and (c) 0.01 % O_2. The mass gain after 500 h for all four ferritic stainless steels is summarized in (d) but the negative mass change for E-brite has been omitted. The average mass from repeated exposures is plotted for the respective test atmospheres and the standard deviation is represented by the error bars.

oxygen, humidified air and humidified hydrogen [21]. They found that the oxidation rate was faster in air and oxygen than in wet hydrogen and concluded that this was due to the increase in oxygen pressure. In contrast, in a study by Ardigo et al., a higher oxidation rate was observed in a simulated fuel electrode environment than in an oxygen electrode environment for the 18% Cr steel AISI 441 [22]. When a higher alloyed steel, Alloy 230, was exposed in the same environments the opposite relation was found in Ref. [23]. In addition, Kurokawa et al. exposed SUS430, a 16% Cr steel, in humid hydrogen and air and did not see any difference in oxidation rate as a function of oxygen pressure [24].

When oxygen partial pressure is discussed, the environments used for low oxygen partial pressures are often generated by mixtures of H_2/H_2O or CO/CO_2. Yet, water, as a reactant itself, has been shown to affect the oxidation behavior of chromia-forming alloys [25–28]. Hydrogen has also been shown to have effects on oxidation [29]. Therefore, the aim of this study is to examine the isolated effect of oxygen pressure on the corrosion of ferritic chromia-forming interconnect steels. The goal was also to obtain fundamental insights into the potential consequences if SOFC stacks are run in SOEC mode. Furthermore, some studies have also shown that operation at elevated pressures, which means higher oxygen concentration, could lead to overall system benefits [30–32]. In this study, the degradation of four commercial ferritic stainless steels was investigated in oxygen pressures ranging from 10^{-4} to 1 atm at 850 °C. Oxidation kinetics, oxide scale evolution and microstructure were investigated and additionally measurements of the evaporation of volatile chromium species were carried out.

2. Experimental

2.1. Sample preparation

The materials studied were Sanergy HT (Sandvik), Crofer® 22 H (ThyssenKrupp), E-Brite® (ATI) and ATI 441HP™ (ATI), all of them

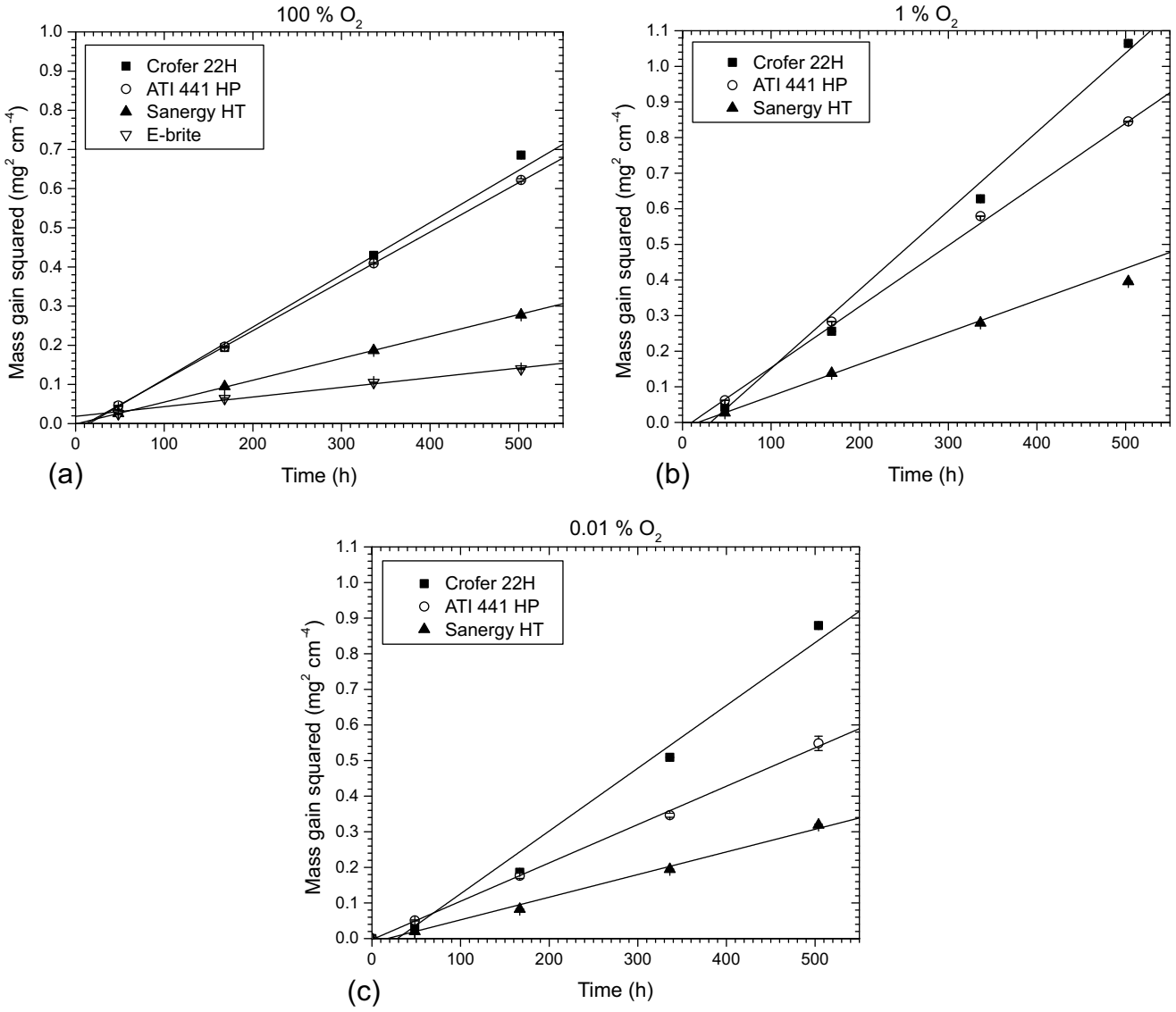

Fig. 2. Parabolic oxidation graphs for the tested ferritic stainless in (a) 100% O_2 (b) 1% O_2 and (c) 0.01 % O_2. The data for E-brite in (b) and (c) has been omitted since the mass gain was negative due to severe spalling of the oxide.

Table 1
Composition of the investigated steels in weight%. The compositions were given by the respective manufactures for the received batches.

Material	Thickness (mm)	Fe	Cr	Mn	Si	Al	Ti	W/Mo	Nb	Zr	La	C	P	S
Sanergy HT	0.2	Bal	21.2	0.30	0.12	0.02	0.09	0.96Mo	0.71	0.21		0.044	0.013	0.001
Crofer® 22 H	0.2	Bal	22.9	0.40	0.20	0.02	n/a	1.9W	0.50	0.024	0.049	0.013	0.02	0.002
ATI E-Brite®	0.5	Bal	26.2	0.07	0.17	0.02	n/a	1.02Mo	0.12			0.0015	0.011	0.0108
ATI 441HP™	0.5	Bal	17.8	0.29	0.38	0.03	0.22		0.50			0.013	0.024	0.0007

ferritic stainless steels. Their compositions can be found in Table 1. The materials were received in the form steel sheets and were cut into $15 \times 15\,mm^2$ samples with a shearing machine. The samples were then washed using ultra-sonic agitation in acetone for ten minutes followed by a wash in ethanol for the same amount of time. The respective surface finish of the material, as stated by the manufacturers, were: Sanergy HT—cold rolled and bright annealed (2R), Crofer 22 H—cold rolled, annealed, quenched and pickled and for E-brite and 441 HP—cold rolled, heat treated, pickled with bright finish (2B). The samples were not ground or polished before exposure.

2.2. Exposures

Exposures of the materials were carried out in horizontal tubular furnaces with an inner diameter of 46 mm. The samples were placed standing in an alumina sample holder parallel to the gas stream. A porous SiC plug was placed upstream of the samples to obtain a more even temperature profile and to limit self-convection of evaporated chromium species. A more detailed description about the exposure setup can be found in Ref. [33]. The concentration of oxygen was varied by mixing different proportions of dry O_2 and Ar, and the total gas flow rate was $1\,sL\,min^{-1}$ in all experiments, which corresponds to a mean flow velocity of $3.8\,cm\,s^{-1}$ inside the furnace tube. The exposures were carried out at 850 °C.

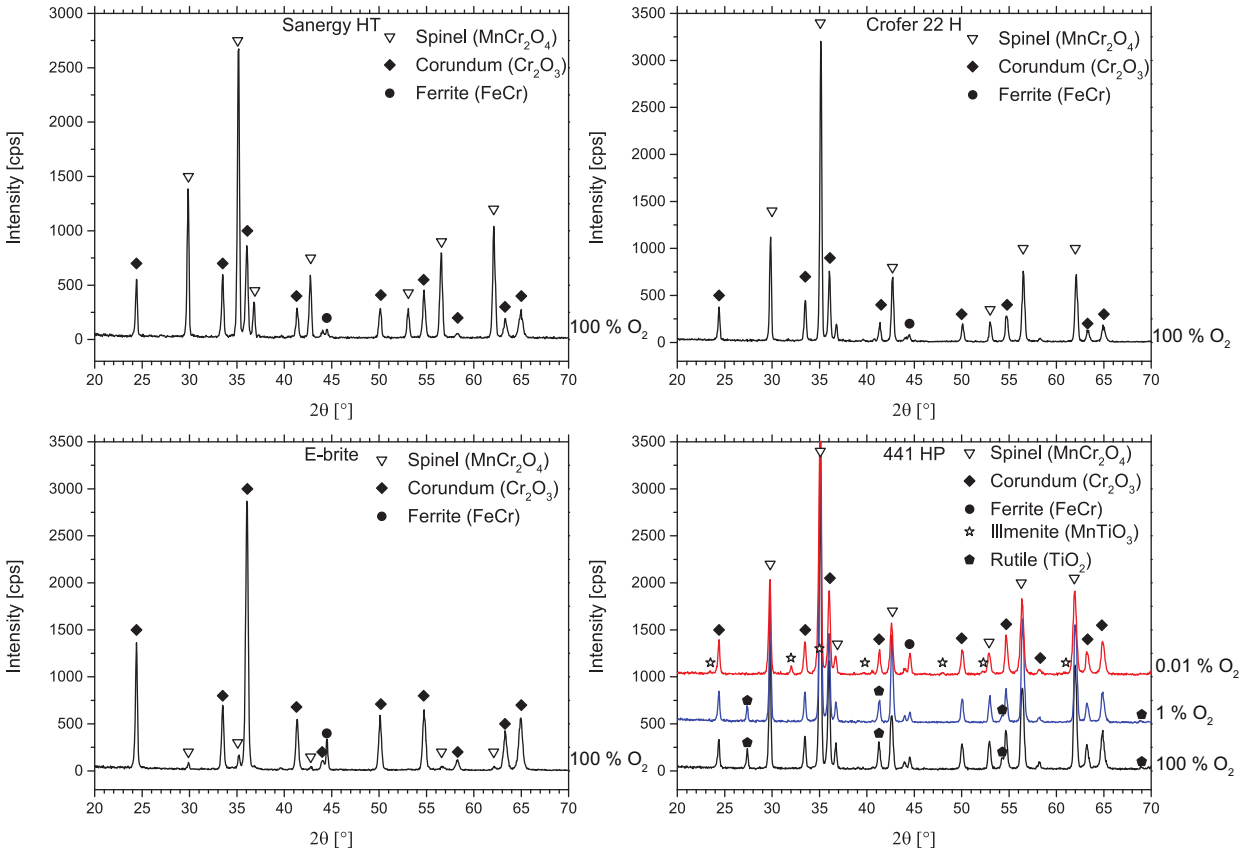

Fig. 3. X-ray diffractograms for all the tested ferritic stainless steels after 500 h of exposure in 100% O_2, and also in 1% and 0.01% O_2 for 441HP.

Exposures in atmospheres of Ar–0.01% O_2, Ar–1% O_2 and 100% O_2 were carried out for 500 h. In each experiment, one sample of each test material was exposed. Experiments were repeated three times for every atmosphere composition. Mass gain was measured at regular intervals to monitor the oxidation rate, and thus the samples were thermally cycled each time the samples were weighed. The samples were flushed with the desired gas composition 1 h before heating was initiated in order to avoid contact with air at high temperature.

2.3. Chromium evaporation measurement

Separate chromium evaporation measurements were performed for Crofer 22 H samples in Ar–25% O_2, Ar–50% O_2, Ar–75% O_2 and 100% O_2 using a denuder technique in which a 6 mm inner diameter tube coated with Na_2CO_3 is placed downstream of the samples. The Na_2CO_3 reacts with gaseous CrO_3 to form Na_2CrO_4, according to Eq. (1), which is then dissolved in water and analyzed using a Thermo Scientific Evolution 60s UV–vis spectrophotometer. Details about this technique can be found in Ref. [33]. The accumulated chromium was measured after 168 h exposure time, and the total flow rate was 1 sL min^{-1} in all exposures.

$$CrO_3\,(g) + Na_2CO_3\,(s) = Na_2CrO_4\,(s) + CO_2\,(g) \quad (1)$$

2.4. Sample analysis

Plan view and cross section images of the samples, as well as compositional information, were obtained using scanning electron microscopy with a FEI Quanta FEG 200 ESEM and a Zeiss LEO ULTRA 55 FEG-SEM equipped with an Inca energy-dispersive X-ray analysis (EDX) system. Cross sections of samples were prepared both by polishing epoxy mounted samples as well as by focused ion beam milling (FIB). Before mounting the samples, a protective layer of metallic Ni was applied by electroplating. The FIB cross sections were prepared with a FEI Versa 3D DualBeam (FIB/SEM). X-ray diffraction was performed on the oxide scales of the exposed samples in a Siemens D5000 diffractometer with a grazing incidence angle of 5–10.

3. Results

3.1. Oxide growth kinetics

The mass change over time is plotted for up to 500 h for all the discontinuous exposures in Fig. 1, and the mass change after 500 h of exposure is summarized in Fig. 1(d). An increase in mass should be directly proportional to the oxygen uptake of an alloy and thus also to the thickness of the oxide, given that no mass losses by, e.g. spalling of the oxide or evaporation is taking place and that the oxide density stays constant. Since the solubility of oxygen in ferritic stainless steels is very low, all the oxygen uptake can be considered to result in the formation of an oxide scale. In general, the rate of oxidation for the tested ferritic stainless steels followed the parabolic rate law according to Eq. (2) where Δm is the change in mass, A is the total sample area, t is the exposure time, k_p is the parabolic oxide rate constant and C is the integration constant which is dependent on the starting conditions [34]. If $\Delta m = 0$ at $t = 0$ then $C = 0$. The mass gain squared for the tested materials is plotted against time in Fig. 2. The corresponding k_p values are given for the tested ferritic stainless steels in their respective exposure atmospheres in Table 2.

$$\left(\frac{\Delta m}{A}\right)^2 = k_p t + C \quad (2)$$

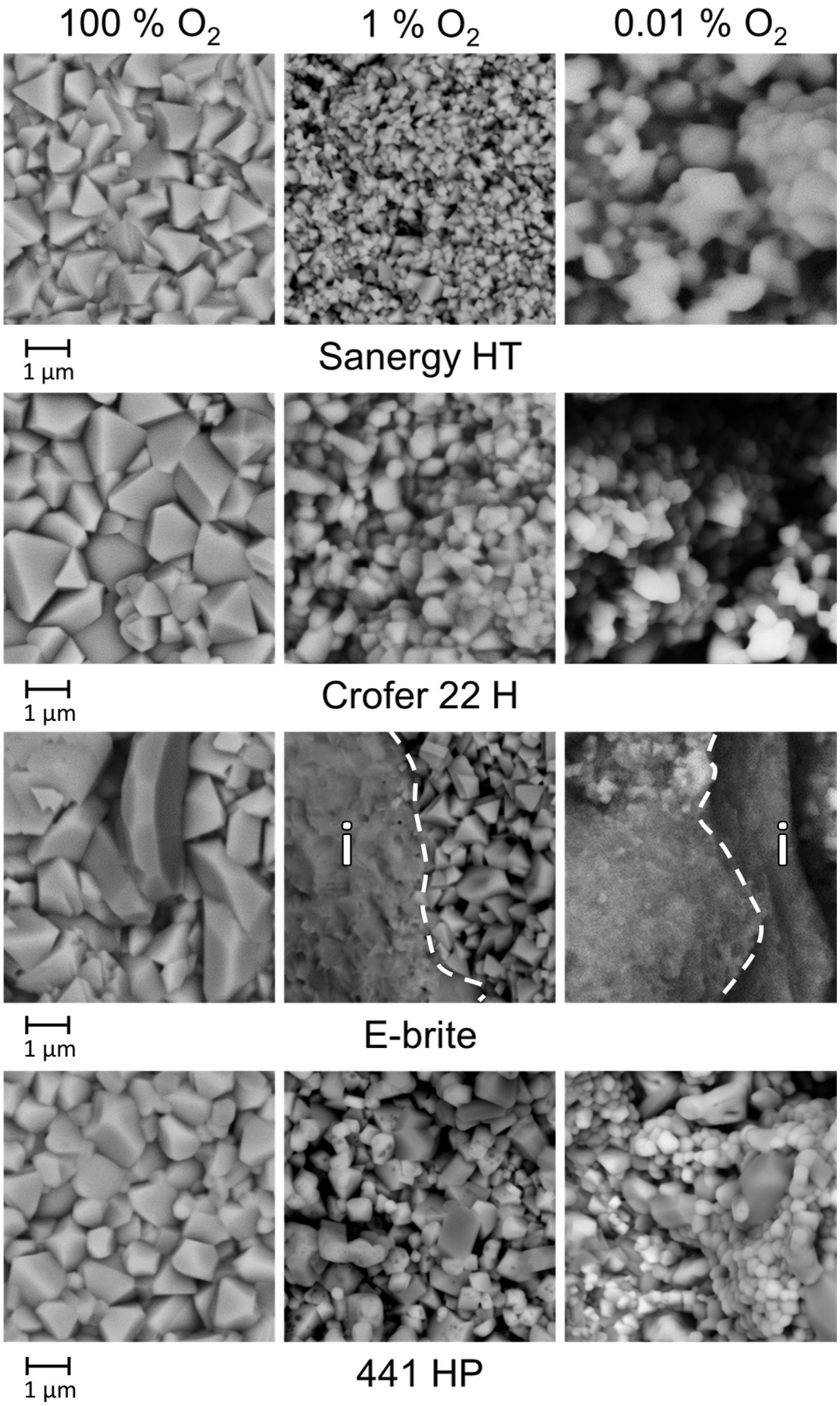

Fig. 4. SEM backscattered micrographs from plan views of Sanergy HT, Crofer 22 H, E-brite and 441HP exposed for 500 h at 850 °C in 100%, 1% and 0.01% O_2. The number (i) represents areas where the oxide has spalled off.

Table 2
Rate constants (k_p) for the studied ferritic stainless steels. Some values have been omitted due to non-parabolic growth rate.

$k_p \times 10^{14}$ [$g^2\,cm^{-4}\,s^{-1}$]				
	Crofer 22 H	441 HP	Sanergy HT	E-brite
100% O_2	38	35	15	8
1% O_2	59	47	22	–
0.01% O_2	49	30	18	–

A deviation from parabolic oxidation kinetics was observed for E-brite which spalled severely after only 48 h of exposure in 0.01% and after 168 h in 1% O_2. In 100% O_2 E-brite exhibited parabolic oxidation kinetics and a mass gain of only 0.37 mg cm^{-2}, which was the lowest of all tested steels, however, after 500 h exposure some oxide spalling was detected using SEM analysis. This indicates that the oxide growth rate for E-brite was slow, but the adhesion of the oxide scale to the metal substrate was poor. Some spalling of the oxide was also detected on some of the 441HP samples exposed in 0.01% O_2. This should result in a small underestimation of the oxidation rate when considering only the mass gain, but the fact that only minor spalling could be detected this is considered to have a very little effect on the measured mass gain. The two materials, Sanergy HT and Crofer 22 H, did not show any signs of spalling of the oxide. Excluding E-brite, Sanergy HT oxidized the slowest in all atmospheres with mass gains ranging from 0.53 to 0.63 mg cm^{-2}. Crofer 22 H had the highest mass gain of the tested steels in all oxygen pressures, ranging from 0.83 to 1.03 mg cm^{-2} after 500 h. The oxidation rate of 441HP was very similar to that of Crofer 22 H, only slightly lower. Considering Fig. 1d, it becomes apparent that the oxidation rate was slightly higher after exposure in 1% O_2 for all materials. In 100% and 0.01% O_2 the oxidation rate was slightly lower, but no significant difference could be observed between these two environments. Thus, there was no clear trend between oxidation rate and oxygen pressure but rather a small maximum in oxidation rate when a sample was exposed to 1% O_2. Since this observation was consistent for all the materials, and since the same test setups were used for all the investigated oxygen pressures, this might be seen as an actual effect of the test atmosphere and not just a statistical coincidence.

3.2. Microstructure

The top surfaces and cross sections of the exposed ferritic stainless steels after 500 h were analyzed with electron microscopy and compositional information was gathered using EDX. Gracing incidence X-ray diffraction analysis was used to analyze the crystal phases of the formed oxides (see Fig. 3). It was found that a spinel phase and a corundum phase were present on all samples, although the spinel signal of E-brite was very weak. EDX analyses in combination with X-ray diffraction of cross sections of the oxides confirmed that all the steels formed an inner layer of Cr_2O_3 (corundum) and an outer layer of $(Cr,Mn)_3O_4$ (spinel), which is in agreement with what has been observed for manganese-containing steels before [11,35–37]. Due to spalling of the oxide and a very thin oxide top layer, it was not possible to analyze the composition of the spinel on the E-brite samples. For Sanergy HT, Crofer 22 H and 441 HP, the spinel composition followed the formula of $Cr_{2-x}Mn_{1+x}O_4$ where x varied between 0.0–0.2. No correlation between spinel composition and oxygen pressure was noted. In general, an almost pure chromia subscale was formed with manganese and iron contents in the range of ≤1 atomic% according to the EDX measurements.

Representative plan view micrographs for Sanergy HT, Crofer 22 H, E-brite and 441HP are shown in Fig. 4. The shape of the crystallites on the surface of Sanergy HT, Crofer 22 H and 441 HP was octahedral which is in agreement with a cubic spinel structure. This

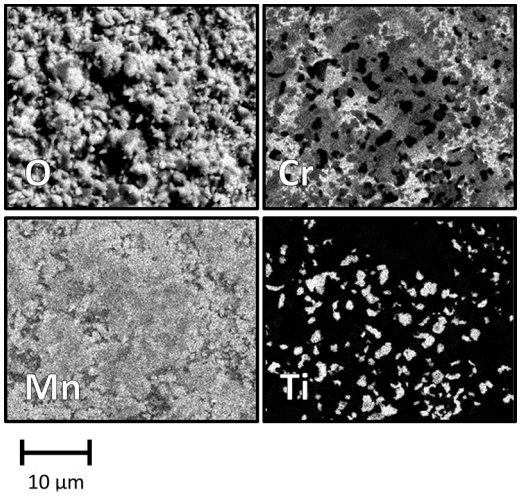

Fig. 5. Elemental EDX maps from a plan view of 441HP exposed for 500 h at 850 °C in 0.01% O_2, showing the presence of ilmenite on the surface of the sample.

was also observed on the E-brite samples exposed in 100% O_2, but elongated crystallites of hexagonal Cr_2O_3 were also detected on those samples, which shows that a spinel layer did not cover the whole sample surface after 500 h of exposure. At exposures in 1% and 0.01% O_2, most of the oxide had spalled off the E-brite samples during cooling. It seems that oxide adhesion is better in 100% O_2 and decreases as towards more diluted atmospheres. The surface morphology of Crofer 22 H was very similar to that of Sanergy HT but with larger crystallites. There was a general trend for all materials to form smaller oxide crystallites on the sample surfaces when exposed in lower oxygen pressures. The size difference was the largest between 100% O_2 and 1% O_2. Between 1% O_2 and 0.01% O_2, the trend towards smaller crystallites was not as clear. In general, the samples exposed in 0.01% O_2 had more uneven topography as opposed to samples exposed in 100% O_2, which had denser and more even surfaces.

The surface morphology of 441HP differed in a number of ways. Some spalling of the oxide was detected after 500 h of exposure in 0.01% O_2. Additionally, titanium-rich oxides were discovered using EDX analysis on samples exposed in all atmospheres. There was a trend to form more and larger titanium oxide crystals in lower oxygen pressures. In Fig. 4, these are visible in the 1% and 0.01% O_2 atmospheres as rod shaped crystals which appear darker in color than the cubic spinel crystals. In 100% and 1% O_2, the titanium oxide phase was identified by XRD analysis (see Fig. 3) to be of rutile structure (TiO_2). In 0.01% O_2, there was a sample to sample variation between rutile structure and ilmenite structure ($MnTiO_3$). In Fig. 5 an SEM/EDX micrograph of the oxide surface of a 441HP sample exposed in 0.01% O_2, on which ilmenite crystallites had formed, is shown.

A micrograph summarizing cross sections of 441HP in all atmospheres after 500 h of exposure is presented in Fig. 6. In the figure, titanium oxide grains are visible for oxides grown in 1% and 0.01% O_2. The total thickness of the oxides varied between 5 and 6 µm. It can be seen how the outer spinel is more even and denser in 100% O_2 and becomes less dense and more irregular in 1% and 0.01% O_2. The spinel was very uneven in thickness in 0.01% O_2 and varied from constituting half of the oxide thickness to being extremely thin at some locations. An example of the latter is shown in the micrograph in Fig. 6. Severe internal oxidation of Ti was detected in all tested atmospheres for 441HP. The bulk structure of the 441HP samples did not vary between atmospheres. In all cases, Laves phase precipitations consisting of mainly Fe-Nb-Si were found mainly within the grain boundaries. More information about Laves phase

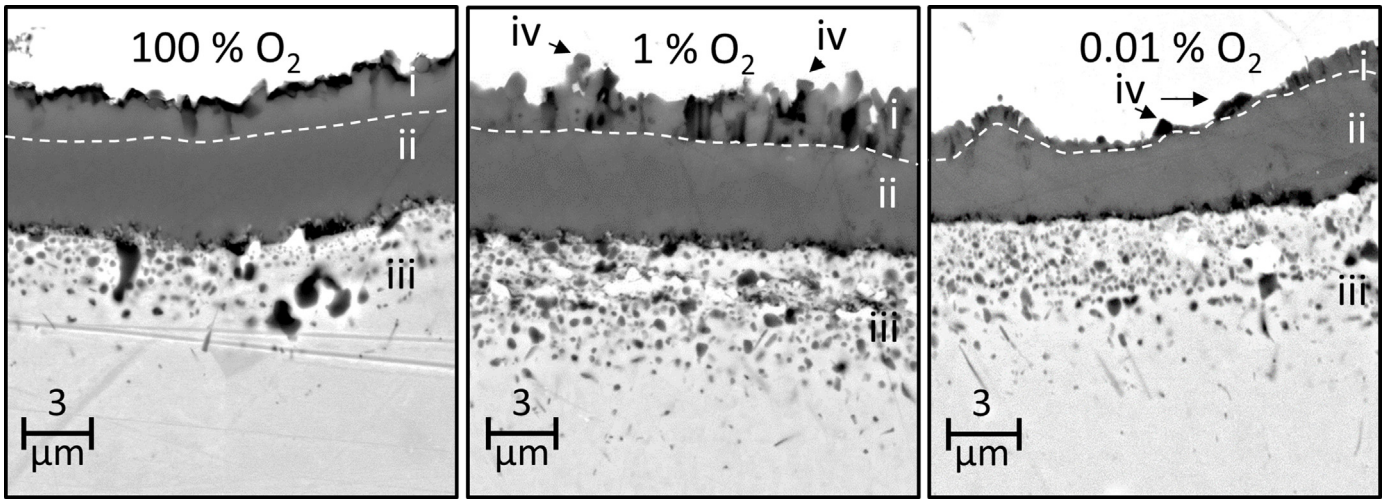

Fig. 6. SEM backscattered micrographs from cross-sections of 441HP exposed for 500 h at 850 °C in 100%, 1% and 0.01% O_2. The numbers represents: (i) $(Cr, Mn)_3O_4$ (ii) Cr_2O_3 (iii) internal titanium oxide (iv) surface titanium oxide.

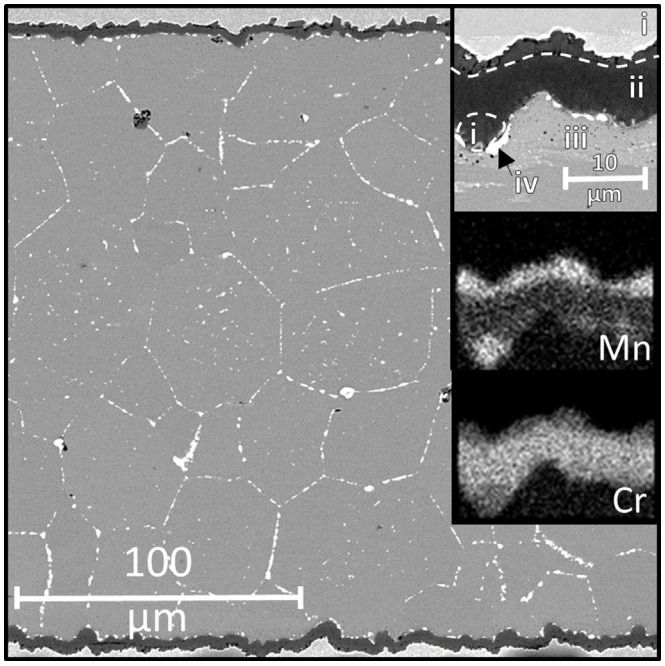

Fig. 7. SEM backscattered micrograph from a cross section of Crofer 22 H exposed for 500 h at 850 °C in 100% O_2. The numbers represents: (i) $(Cr, Mn)_3O_4$ (ii) Cr_2O_3.

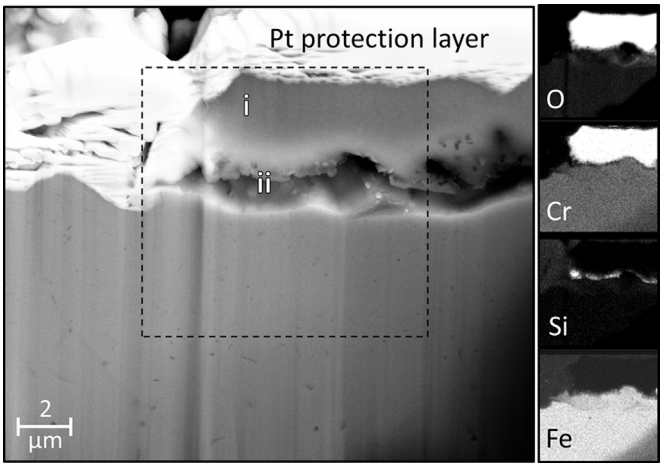

Fig. 8. Micrograph and elemental EDX maps from a FIB cross section of E-brite exposed for 500 h at 850 °C in 0.01% O_2. The numbers represents: (i) Cr_2O_3 (ii) silica sub-scale.

precipitation can be found in Refs. [35,38,39]. Laves-phase precipitation in the grain boundaries was detected also on samples of the other tested ferritic stainless steels, except for E-brite which can be explained by its low niobium content.

Fig. 7 shows a cross section of a representative Crofer 22 H sample, which has been exposed in 100% O_2 for 500 h. Crofer 22 H samples had the most Laves phase formation of all the tested steels. Underneath the top layer of $(Cr,Mn)_3O_4$ and Cr_2O_3 of the Crofer 22 H, patches of manganese-chromium rich oxide were detected, which can be presumed to be $(Cr,Mn)_3O_4$. The oxide scale/metal interface on this sample was very uneven, which was found to be a result of the rolling of the steel during manufacturing (the samples were not polished before exposure). A 90 cross section of the same sample was prepared to confirm this, which showed a much flatter interface.

Due to weak adhesion of the oxide scale on the E-brite samples it was difficult to prepare traditional mechanically polished cross sections. Instead, one of the E-brite samples, which exhibited severe spalling of the oxide, was chosen for investigation with FIB/SEM. A cross section of E-brite exposed in 0.01 % O_2 for 500 h was prepared by FIB milling and is shown in Fig. 8, including elemental maps from EDX. The cross section stretches from an area where the oxide has spalled off and only bare metal remains, and into an area where an oxide flake still remains. On this particular flake, no manganese was detected. However, it cannot be ruled out that $(Cr, Mn)_3O_4$ was not formed during the first exposure cycle, and the analyzed oxide was formed by re-oxidation of the surface in a later cycle, which would be more depleted of manganese. The manganese content is significantly lower in E-brite than in the other investigated steels (see Table 1) and has previously been reported to only form a very thin $(Cr, Mn)_3O_4$ layer, with high chromium oxide evaporation rate as a consequence [40]. Underneath the chromia scale of the investigated E-brite sample, a continuous silica layer was detected. This is in agreement with what other authors have reported before [21,40]. Some internal oxidation of titanium was also observed as well as internally oxidized needle-shaped alumina.

In order to investigate if the grain size in the underlying chromia scale varied with oxygen pressure, focused ion beam (FIB) milled cross sections of Sanergy HT were prepared and are shown in Fig. 9. The general trend was a smaller grain size with lower oxygen pres-

sure. Similar to the observation of the outer spinel grain size, the largest difference in grain sizes for the inner chromia scale was between the samples exposed in 100% and 1% O_2. In the first quadrant of Fig. 9, a micrograph of the double-layered oxide, as well as the internal titanium oxide formed in 100% O_2 for Sanergy HT, is shown. Spinel thicknesses on the Sanergy HT samples were on average around 1.5 μm, and the total oxide thicknesses were around 4 μm. As with 441HP, the spinel microstructure went from more dense and even in 100% O_2 to more porous in 1% O_2 and more uneven in 0.01% O_2.

3.3. Chromium evaporation

Chromium evaporation of Crofer 22 H, as a representative example, was measured in atmospheres containing 25–100% O_2, and the accumulated chromium evaporation after 168 h is plotted against oxygen pressure in Fig. 10. It should be noted that two measurements were performed at 50% O_2 and the values were identical, consequently they show as one data point. The chromium evaporation showed a linear correlation to oxygen pressure under the tested conditions. In 100% O_2, an average value of 5.9×10^{-3} mg cm^{-2} evaporated chromium was measured after 168 h. This can be compared to a value of 4.8×10^{-2} mg cm^{-2} for the same steel after 168 h of exposure in a simulated SOFC environment with air −3 % H_2O at 850 °C [41].

4. Discussion

4.1. Diffusion and defects in chromia

All tested ferritic stainless steels except E-brite exhibited parabolic oxidation rate over the whole tested oxygen pressure range. According to Wagner theory, this indicates that the diffusion through the oxide scale is rate controlling for oxidation. Thus the oxidation rate should be determined by the defect structure of the oxide [42]. Extensive studies on the mechanisms behind defects in chromia have been carried out by several authors [43–47]. These kinds of measurements are carried out on sintered or hot-pressed pellets or single crystals of Cr_2O_3. In order to understand the dominant defect chemistry, electrical conductivity is often measured as a function of oxygen pressure. Common for p-type oxides is that the number of defects, and consequently the ionic and electric conductivity of the oxide, increases with higher oxygen pressures. For n-type oxides, the conductivity instead has a negative correlation

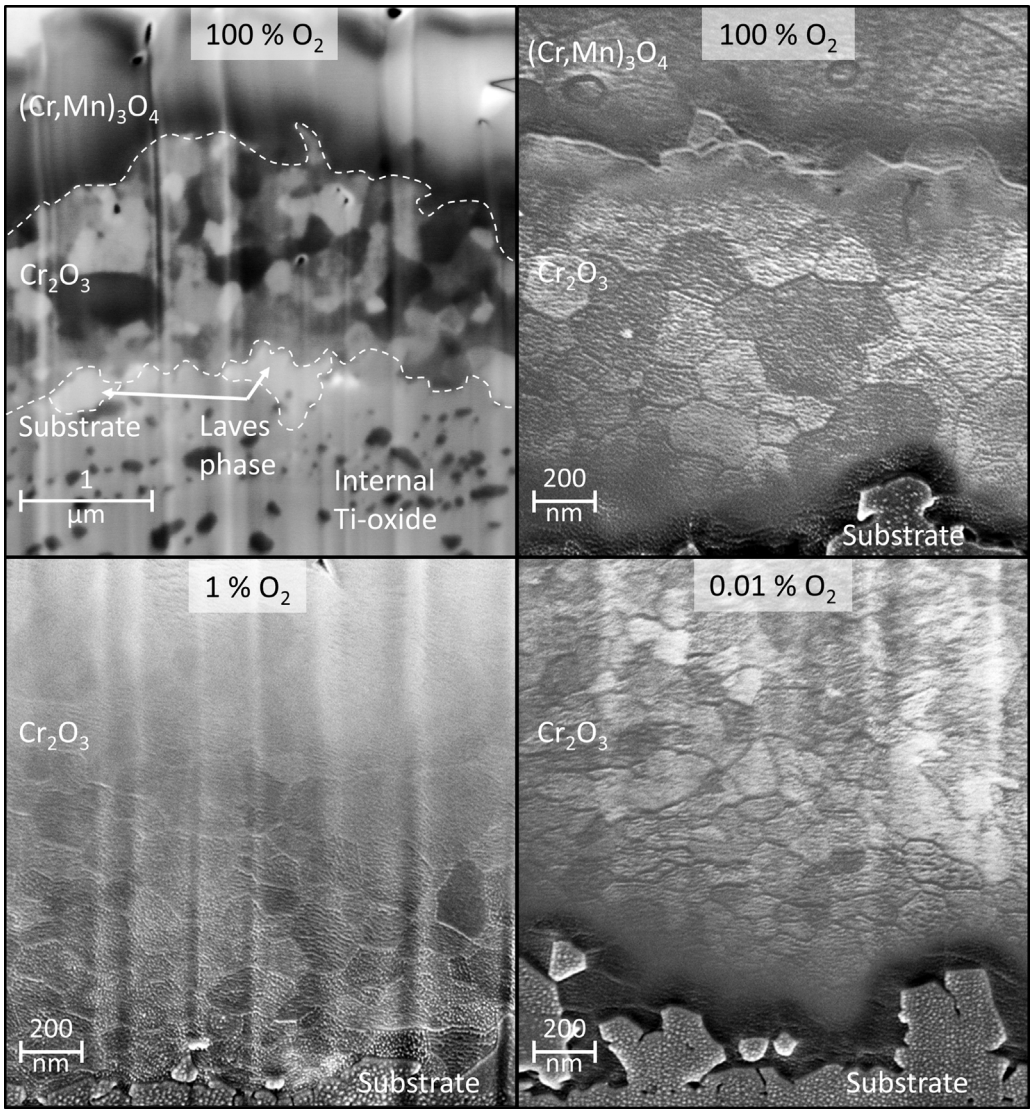

Fig. 9. SEM micrographs from cross sections of Sanergy HT exposed for 500 h at 850 °C in 100%, 1% and 0.01% O_2. The images were acquired with an In-lens SE detector at an accelerating voltage of 3 kV.

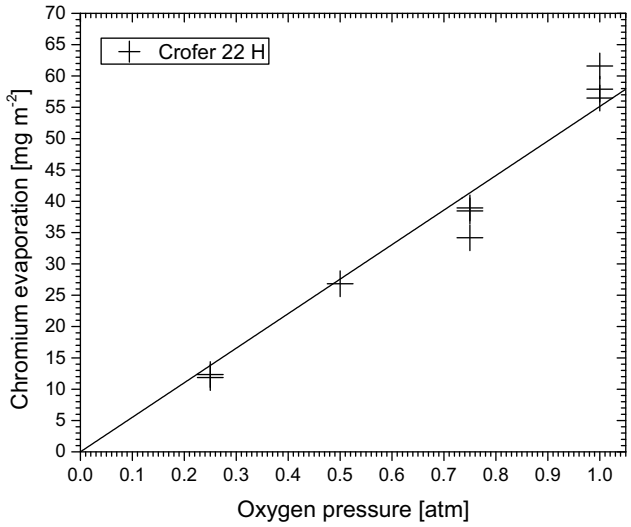

Fig. 10. Accumulated evaporated chromium for Crofer 22 H after 168 h as a function of oxygen concentration in the gas stream at 850 °C with a total flow rate of 1 sL min^{-1}.

to oxygen pressure [48]. At low temperatures (<1200 K), chromia is not considered to be an intrinsic semiconductor and its conduction behavior is generally determined to be of a p-type nature [44–46]. At lower oxygen pressures, close to the dissociation pressure of chromia, a change to n-type behavior has been observed [34,45]. Hagel and Seybolt have shown, using tracer studies that chromium diffusion is predominant in chromia and that oxygen diffusion can be neglected [49]. Thus the dominant defects should either be metal vacancies or metal interstitials which corresponds respectively to p- and n-type oxides. Regarding conductivity, very low dependence on oxygen pressure has been reported in several studies, in order of being proportional to $pO_2^{1/20}$ [44,47]. This is smaller than can be explained by models of predominant point defect structures in unstoichiometric crystals. Holt and Kofstad have suggested that the low measured dependence could be due to the slow equilibration of the defect structures in the specimen and is consequently a kinetic effect [47].

4.2. Oxide scale growth

The general trends in oxide growth behavior as a function of oxygen pressure observed in this study can be summarized as (i) a low dependence for oxidation rate, (ii) a reduction in oxide grain size at lower pressures for both the outer spinel and inner chromia and (iii) a tendency to spall more with lower oxygen pressure. These points will be discussed in this order below. The parabolic rate constant, k_p, should be proportional to the number of defects in the oxide and consequently, if the dominant defect structure is known, the dependence of the oxide growth rate should be able to be predicted as a function of the oxygen pressure. If the diffusion mechanism is dominated by chromium vacancies (p-type), the rate constant k_p should be proportional to the oxygen pressure according to Eq. (3) [48,50,51].

$$k_p = C_1 \left[pO_2(\text{gas})^{1/n} - pO_2(\text{interface})^{1/n} \right] \quad (3)$$

where C_1 is a constant, pO_2(gas) the oxygen partial pressure at the oxide/gas interface and pO_2(interface) the oxygen partial pressure at the metal/oxide interface and n depends on the dominant mechanisms by how the defects are created, e.g. the charge of the vacancies in this case. If the dominant diffusion mechanism instead is through metal interstitials the expression becomes [48,50,51]:

$$k_p = C_2 \left[pO_2(\text{interface})^{-1/n} - pO_2(\text{gas})^{-1/n} \right] \quad (4)$$

In other words, it is negatively proportional to oxygen pressure, as discussed above. But since pO_2(gas) can, in most cases, be considered to be much higher than the dissociation pressure pO_2(interface), the last term in (4) can be omitted and k_p becomes only dependent on the dissociation pressure, which is constant at constant temperature. Through this reasoning, a metal excess chromia scale (n-type) should be independent of ambient oxygen pressure according to Eq. (4). By the same reasoning, the oxidation rate is expected to be dependent on the ambient pressure if it is metal deficient (p-type).

Large differences in diffusivity in single crystals compared to multi-grained chromia pellets have led to the conclusion that diffusion through grain boundaries is several orders of magnitude faster than bulk diffusion within the temperature ranges where chromia forming alloys are used [34,51,52]. This makes it most relevant to discuss the diffusivity within grain boundaries, which have a more complex and less understood structure and chemistry than the bulk. Chromia scales are generally considered to mainly grow outwards in dry atmospheres of oxygen, but with some inward diffusion of oxygen, resulting in lateral growth and compressive stresses in the outer region of the scale [53,54]. The inward diffusion of oxygen has been suggested to be predominantly transported through micro pores and channels in the oxide scale [55,56].

After an extensive review of the literature on electrical properties and diffusion in chromia, complemented with their own studies on thermally grown chromia scales on pure chromium at different temperatures in dry oxygen ranging from 9×10^{-6} to 1 atm Lillerud and Kofstad suggested a model for transport in chromia scales [56,57]. This model is based on the observation that chromia has n-type behavior in oxygen pressures close to its dissociation pressure and the majority defects are presumed to be chromium interstitials. It is then assumed that this structure dominates a majority part of the total oxide scale which should make the oxidation rate independent of the oxygen pressure. In the model suggested by Lillerud and Kofstad bulk diffusion is considered, but as discussed by Polman et al. [51], if the dominant transport mechanisms in grain boundaries is assumed to be the same as in the bulk, the model could still be applied when oxide growth is dominated by grain boundary diffusion. Their model is in agreement with what has been observed in the current study, i.e. no pronounced dependence was found for the oxidation rate on oxygen pressure. Brylewski et al. exposed SUS 430 in simulated anode and cathode atmospheres and did not see any difference in oxidation rate [58]. They have suggested that this n-type behavior is due to the fact that at temperatures lower than 1100 °C the diffusion constant for chromium interstitials far exceeds that of chromium vacancies even though both are present in the chromia scale. Thus the diffusion rate is governed by the chromium interstitial concentration, which is independent of oxygen pressure. Such a model would result in the same independence for k_p as the model suggested by Kofstad and Lillerud. The calculations for k_p as function of oxygen partial pressure by Kurokawa et al. also show that k_p is almost independent of pO_2 at temperatures up to 1000 °C [24]. This is in agreement with the findings of those authors for the oxidation of SUS 430 in simulated air and 97% H_2/3% H_2O anode gas at 800 °C. Thus they concluded that the predominant defect in the chromia scale was chromium interstitials, i.e. n-type behavior in both atmospheres. However, this model is not supported by Palcut et al., who found that the oxidation rate for a number of ferritic stainless steels increased as a function of oxygen pressure when the exposure atmosphere was changed from 9%

H_2/11% H_2O to air/3% H_2O and 100% O_2 at 850 °C. We fail to explain the discrepancy of these results and the results of the current study in any other way than that different gases were used. In the present study dry O2 and Ar were used, whereas Palcut et al. also included water and hydrogen in their exposure environment. It has been shown that the presence of water vapor and hydrogen affects the mechanisms for oxidation. For instance, water vapor might have beneficial effects on the adhesion of the oxide scale to the metal substrate and thus improve corrosion resistance [11]. In case of high gas flow, water in the gas stream can also be detrimental in combination with oxygen since the accelerated chromium evaporation can cause break away oxidation [59]. The presence of water vapor can also change the transport process in the oxide scale, which was shown by Essuman et al. [25]. Srisrual et al. have also shown, using photoelectrochemical measurements on chromia scales grown on Fe23Cr coupons for 60 min at 850 °C in oxygen, that the behavior of chromia acts as p-type semiconductor, but samples oxidized in water vapor showed, in contrast, n-type or insulator behavior [27]. Calculations by Polman et al. show that the surface coverage of adsorbed O_2 molecules in H_2/H_2O-environments at 900 °C, resembling simulated fuel electrode atmospheres, is too low to account for the observed oxidation rate unless H_2O acts as an oxidant [55]. Hydrogen has also been shown to affect chromia scales. Studies by Holt and Kofstad have shown that hydrogen affects the electrical conductivity of chromia and consequently the oxide defect structure [47]. Tveten et al. have shown that chromium is oxidized differently if the metal contained hydrogen before starting exposures in oxygen [29]. These examples show that the discussion of pO_2 dependence on the oxidation behavior, when comparing water and hydrogen containing atmospheres with dry oxygen or air exposures, should take into account the fact that many mechanisms are at play which might give rise to trends that are not an absolute effect of oxygen pressure.

In the discussion above, the growth of the chromia scale is considered, but on all samples an outer layer of $MnCr_2O_4$ spinel was formed as a result of the vastly faster diffusion rate of manganese than chromium and iron through chromia [52]. Thus it is necessary to consider if this results in significantly lower oxygen pressure at the spinel/chromia interface which could in such case explain the independence of the oxidation rate on oxygen pressure. Studies on the oxidation of pure cobalt have shown that when the oxygen pressure in the exposure atmosphere is sufficiently high to form Co_3O_4 on top of CoO the oxidation rate becomes independent of oxygen pressure since the oxygen pressure above CoO will remain constant at the dissociation pressure of Co_3O_4 [48]. However, this is not the same situation as when $MnCr_2O_4$ forms on top of Cr_2O_3. Since the dissociation pressure for $MnCr_2O_4$ is lower than for Cr_2O_3, obviously, the spinel/chromia interface is not in thermodynamic equilibrium. This means that the pO_2 at the spinel/chromia interface is a function of oxygen diffusivity through the spinel and of the ambient oxygen pressure. Since the chromia grows underneath the spinel, it is obvious that there is significant inward diffusion of oxygen through the spinel scale. Chromium manganese spinel top-layers on chromia have not proven to offer any reduction in oxidation rate [40], thus it can be assumed that this spinel layer is essentially oxygen transparent. Consequently, the discussion about the oxygen dependence of chromia-forming alloys should be applicable also when a top-layer of manganese chromium spinel is present, if the growth of the chromia makes up the majority of the total scale growth. In this study it was found that, depending on the manganese content in the investigated ferritic stainless steel, the manganese chromium spinel constituted around one fourth of the scale after 500 h of exposure. It is assumed that only very limited growth of the spinel phase scale will continue after this point due to depletion of manganese in the steel bulk, according to previous studies [40,60]. In other words, to further study the isolated growth of chromia longer exposures should be carried out.

Another factor to take into consideration when comparing mass gains in different oxygen pressures is the increase in chromium evaporation at higher oxygen partial pressure, which results in a lower measured mass gain compared to the actual oxidation rate. However, the measured chromium evaporation for Crofer 22 H in 100% O_2 resulted in a mass loss in the order of 1% of the total measured mass gain and can thus be neglected when comparing the oxidation rates in this study.

A difference in the size of the formed surface crystallites was detected in all the materials (see Fig. 4), and the tendency was that smaller grains were formed in lower oxygen pressure. It was also found that the grain size of the chromia layer of Sanergy HT samples also decreased in lower oxygen pressure. It can be assumed that the same trend is followed by the other investigated ferritic stainless steels as well. Palcut et al. also observed larger grain sizes with increasing oxygen pressure [21]. They explained this observation to be due to a faster oxidation rate. However, the same phenomenon was observed in the present study even though the oxidation rates were basically unchanged when the oxygen pressure was changed. The trend of increasing grain size with increased oxygen pressure was also observed by Lillerud and Kofstad for chromia grown on pure chrome in dry oxygen atmospheres at 800–1000 °C [57]. They also observed that the plasticity of the chromia scale increased in decreasing oxygen pressure, which, due to the compressive stresses in growing chromia, resulted in more deformed and uneven scales. From these observations those authors suggested that the ability to creep increases with decreasing oxygen pressure due to higher oxygen vacancy concentration [56]. As discussed by Lillerud and Kofstad, the oxygen gradient over the scale should thus cause the inner parts of the scale to be more plastic and the outer parts to be more rigid. At reduced oxygen pressure in the atmosphere, the ability for an oxide scale to deform should increase but could yet cause micro cracks in the outer regions. This should result in new sites for grain nucleation and consequently smaller grain size. This does not, however, explain why the grain size of the chromia at the metal/oxide interface is also reduced at lower oxygen pressure, as observed for the Sanergy HT samples. In agreement with the suggested model, Lillerud and Kofstad noted that chromia scales had a greater tendency to detach from the metal and form gaps at the interface. Such mechanism could explain the increased tendency for the oxide to detach at lower oxygen pressure which was observed for the 441HP and E-brite samples. If the ability increases at lower oxygen pressure, as suggested by Lillerud and Kofstad, the oxide scale could experience more tension when being cooled down to room temperature.

Oxide scales formed on Sanergy HT and Crofer 22 H are expected to have better adherence due to the reactive element effect owing to the presence of Zr in Sanergy HT and La in Crofer 22 H in the steels [61]. The severe spalling of the oxide scale seen on the E-brite samples was likely caused by the formation of a continuous silica layer at the metal/oxide interface (see Fig. 8), due to the considerably lower thermal expansion coefficient of silica compared to the steel [11]. Silica precipitation underneath the chromia scale of E-brite has also been reported by other authors [21,40]. Compared to the composition of the other tested ferritic stainless steels, E-brite had the highest ratio of Si/Nb. Niobium is known to tie up silicon in Laves phases and decrease the tendency for silica formation at the metal/oxide interface [62]. Thus oxidation properties could be expected to be improved by a higher amount of niobium in E-brite.

Another observation of microstructural changes as a function of oxygen pressure was the tendency for more titanium oxide precipitates at the surface of the oxides grown on 441 HP. Compared to the other tested steels, 441 HP has a considerably higher titanium content. This also explains the extensive internal oxidation zone on

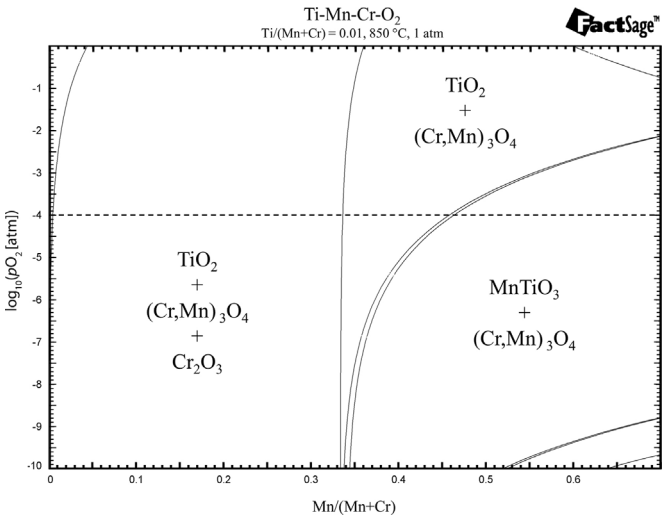

Fig. 11. Calculated phase diagram for a Ti–Mn–Cr–O_2 system by FactSage™ (FACT oxide database) [63].

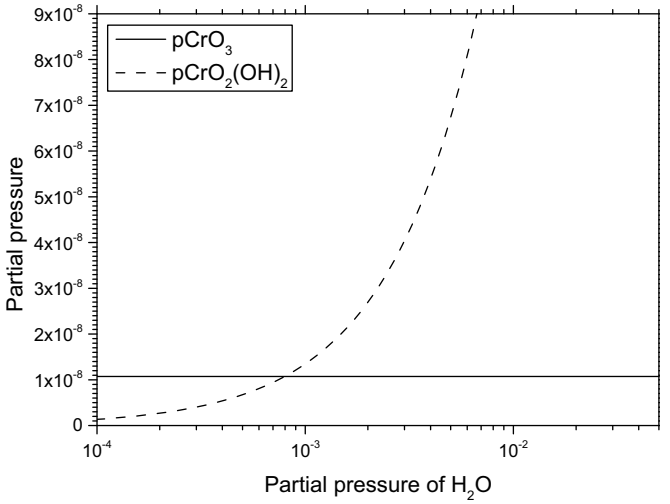

Fig. 12. Partial pressures of CrO_3 and $CrO_2(OH)_2$ in equilibrium over Cr_2O_3 (s) at 850 °C in an O_2 atmosphere as a function of water vapor contamination. The thermodynamic data for CrO_3 was taken from Ref. [69] and for $CrO_2(OH)_2$ from Ref. [68].

the 441 HP sample compared to the other steels, which is a result of the extremely low dissociation pressure of titanium oxides. It was also noted that the titanium oxides that formed on top of the chromium manganese spinel in 100% and 1% O_2 were TiO_2 and in 0.01% O_2 a mix of TiO_2 and $TiMnO_3$. This phase change is supported by thermodynamic calculations conducted for a Cr-Mn-Ti-O_2 system in the software FactSage™ [63], as can be seen in the phase diagram in Fig. 11. This phase diagram was calculated for a cation concentration for titanium of 1 at% and it can be seen that a phase transition from TiO_2 to $TiMnO_3$ occurs when the oxygen pressure is reduced and the manganese content is increased. The mixed results for the formation of TiO_2 and $TiMnO_3$ in 0.01% O_2 suggests that this oxygen pressure is in a transition region, and that small variations of manganese in the spinel top oxide could result in either phase. The trend for higher titanium concentrations at the oxide/gas interface in lower oxygen pressure was also observed by Essuman et al. for a NiCr base alloy [64]. It is likely that this is caused by higher solubility of titanium in the chromia and chromium manganese spinel oxide scales, which allows for faster transport of titanium to the surface [64,65]. More titanium within the chromia scale is suggested to cause an increase in the oxidation rate due to doping [66,67]. However, such a model is not supported by the findings in this study since there is no pronounced trend that shows an increase in oxidation rate with a decrease in oxygen pressure. Such trend should also be more pronounced for 441HP than for the other steels in the study, since it has the highest titanium content, but this was not observed.

4.3. Chromium evaporation

The evaporation of chromium from interconnect steels has been measured in humidified air, which resembles the oxygen electrode environment of a SOFC, by several authors, as seen in the review of Key et al. [17]. The dry oxygen used in this study should more closely resemble the conditions at the oxygen electrode in a SOEC stack. Chromium evaporation from ferritic stainless steels in simulated SOEC environments are not commonly presented in the literature. The rate of chromium evaporation in a dry atmosphere is expected to be significantly lower than in a water containing atmosphere, since the formation of gaseous $CrO_2(OH)_2$ is not possible [68]. In dry oxygen at 850 °C, the major Cr vapor species is CrO_3 which is formed according to Eq. (5) [69].

$$\frac{1}{2}Cr_2O_3\,(s) + \frac{3}{4}O_2\,(g) = CrO_3\,(g) \tag{5}$$

Thus, according to Eq. (5), the evaporation rate should be proportional to $\propto pO_2^{0.75}$ under equilibrium conditions. Since the dependence of the evaporation rate on the oxygen pressure was observed to be linear in this study, it can be concluded that the gas speed of 3.8 cm s^{-1} represents a flow region which is, at least partly, kinetically controlled. A separate study on flow rate would be required in order to determine if the reaction is in a totally kinetically controlled flow region or not, i.e. where the evaporation rate is independent of flow rate. However, by comparison with flow rate studied by Froitzheim et al. on the evaporation of $CrO_2(OH)_2$, total flow rate independence seems unlikely, and a significantly higher flow rate should be required to reach a fully kinetically controlled region [33].

Moreover, the measured rate of chromium evaporation in dry oxygen was in the same range as interconnect steels with applied protective coatings, like Co/Mn spinels, in humid air atmospheres [17]. Nevertheless, chromium contamination of oxygen electrodes has been suggested to be a major cause of degradation in SOEC stacks [70]. It seems unlikely that such severe chromium evaporation could occur in the dry oxygen environment in a SOEC judging from the low levels measured in this study. Tucker et al. have claimed that a substantial amount of chromium transport from the interconnects to the electrode can occur through solid state surface diffusion [71]. Another possible explanation is that the leakage of hydrogen between the cathode and anode sides results in an elevation of water concentration on the oxygen side. In such a case, the chromium evaporation rate will be severely underestimated if the humidity level is not considered. To illustrate this, the vapor pressures of $CrO_2(OH)_2$ and CrO_3 have been plotted against humidity level in oxygen at 850 °C in Fig. 12. The thermodynamic data for $CrO_2(OH)_2$ and CrO_3 was taken from Opila et al. and Ebbinghaus, respectively [68,69]. It can be concluded that above a water concentration of 0.1% (approx. −20 °C frost point), the predominant chromium vapor species is $CrO_2(OH)_2$. In other words, since pure oxygen, compared to air, is produced in SOECs, this means that even very small leakages of hydrogen can lead to significant chromium evaporation and it cannot be ruled out that barrier coat-

ings against chromium migration are necessary in SOEC as well as in SOFC applications.

4.4. Material performance

For an alloy to be suitable as interconnect material in an SOEC or SOFC, it is crucial that the oxide scale of the alloy remains well adherent during the operating life time of the stack since delamination will result in lost electrical contact. By comparing the performance of the tested ferritic stainless steels, it can be concluded that E-brite has too great a tendency for spalling of the oxide scale to be suitable as interconnect material in uncoated form in the tested environments. Signs of spalled oxide were also observed for 441HP after 500 h of exposure, which would be insufficient for long-term operation at 850 °C. The reactive element-containing steels, Crofer 22 H and Sanergy HT, performed better in terms of scale adhesion. Nevertheless, the oxidation rate can be assumed to be too high for long-term operation. Liu et al. performed a life time prediction study on Crofer 22 APU and concluded that at a scale thickness of around 11 μm there is high risk of spalling of the oxide scale [15]. Using this thickness and the calculated k_p values in Table 2, it is possible to qualitatively calculate expected lifetimes for the steels tested in this study using the density for pure Cr_2O_3 and assuming a perfectly dense scale. For Crofer 22 H in 100 % O_2 at 850 °C, this leads to an estimated life time of 2000 h and for Sanergy HT 5000 h. Since relatively short term data has been used for these extrapolations, they should only be seen as an indication of the life time that can be expected. However, it can be assumed that the oxidation rates for all the steels in this study are too fast if the commonly mentioned 40 000 h operation is the technical target [72]. It has been shown that the oxide scale adherence to a steel and the oxidation rate can be significantly improved by applying reactive element coatings [13,18,60]. This, in combination with lower operating temperatures, should significantly increase the lifetimes of the steels and enable the use of the tested steels [41].

5. Conclusions

The effect of changing oxygen pressure in a dry atmosphere at 850 °C was investigated for a number of commercial ferritic stainless steels. The oxidation rate was not found to vary substantially with oxygen pressure in the range of 10^{-4} to 1 atm. Oxidation kinetics was parabolic which leads to the conclusion of a diffusion-controlled oxidation process. The oxidation rate for all steels was too high for long term operation in SOEC applications. The most pronounced effect of changing oxygen pressure was found for the microstructure of the oxide scales. Both the inner Cr_2O_3 and the outer $MnCr_2O_4$ spinel consisted of smaller grains when exposed to lower oxygen pressure. Furthermore, a tendency towards a decrease in oxide scale adhesion was also observed when the oxygen pressure was reduced. This effect was only observed for E-brite and 441HP, which both lack reactive elements. Chromium evaporation was recorded to be significantly lower in a simulated SOEC atmosphere than in a simulated SOFC atmosphere. At a gas flow rate of 3.8 cm s^{-1}, the chromium evaporation rate increased linearly with oxygen pressure, which indicates that the gas flow was too fast to reach equilibrium concentration in the gas stream.

Acknowledgements

The financial support received from The Swedish Research Council and Swedish Energy Agency and The Swedish High Temperature Corrosion Centre is gratefully acknowledged. Itai Panas, Jan Grolig and Christine Geers aided in the completion of this paper through fruitful discussions and great support, thank you. Furthermore, we acknowledge the steel manufacturers, Sandvik Materials Technology, ATI Metals and VDM Metals for providing the test materials.

References

[1] I. Staffell, A. Ingram, K. Kendall, Energy and carbon payback times for solid oxide fuel cell based domestic CHP, Int. J. Hydrogen Energy 37 (2012) 2509–2523, http://dx.doi.org/10.1016/j.ijhydene.2011.10.060.
[2] F. Baratto, U.M. Diwekar, Life cycle assessment of fuel cell-based APUs, J. Power Sources 139 (2005) 188–196, http://dx.doi.org/10.1016/j.jpowsour.2004.07.025.
[3] N. Minh, Solid oxide fuel cell technology—features and applications, Solid State Ionics 174 (2004) 271–277, http://dx.doi.org/10.1016/j.ssi.2004.07.042.
[4] F. Calise, A. Palombo, L. Vanoli, Design and partial load exergy analysis of hybrid SOFC–GT power plant, J. Power Sources 158 (2006) 225–244, http://dx.doi.org/10.1016/j.jpowsour.2005.07.088.
[5] S.D. Ebbesen, M. Mogensen, Electrolysis of carbon dioxide in solid oxide electrolysis cells, J. Power Sources 193 (2009) 349–358, http://dx.doi.org/10.1016/j.jpowsour.2009.02.093.
[6] M.a. Laguna-Bercero, Recent advances in high temperature electrolysis using solid oxide fuel cells: a review, J. Power Sources 203 (2012) 4–16, http://dx.doi.org/10.1016/j.jpowsour.2011.12.019.
[7] J.A. Turner, Sustainable hydrogen production, Science 305 (2004) 972–974.
[8] S.C. Singhal, K. Kendall, Introduction to SOFCs, in: High Temp Solid Oxide Fuel Cells, Elsevier, 2003, pp. 1–22, http://dx.doi.org/10.1016/B978-185617387-2/50018-0.
[9] J. Larminie, A. Dicks, Fuel Cell Systems Explained, John Wiley & Sons, Ltd., West Sussex, England, 2003.
[10] T.D. Hall, H. McCrabb, J. Wu, H. Zhang, X. Liu, J. Taylor, Electrodeposition of CoMn onto stainless steels interconnects for increased lifetimes in SOFCs, in: Solid Oxide Fuel Cells 12 (SOFD XII), Electrochemical Society Inc., 65 S Main ST., Pennington, NJ 08534-2839, USA, 2011, pp. 2489–2502, http://dx.doi.org/10.1149/1.3570247.
[11] W.J. Quadakkers, J. Piron-Abellan, V. Shemet, L. Singheiser, Metallic interconnectors for solid oxide fuel cells—a review, Mater. High Temp. 20 (2003) 115–127, http://dx.doi.org/10.3184/096034003782749071.
[12] K. Huang, Characterization of iron-based alloy interconnects for reduced temperature solid oxide fuel cells, Solid State Ionics 129 (2000) 237–250, http://dx.doi.org/10.1016/S0167-2738(99)00329-X.
[13] J.G. Grolig, J. Froitzheim, J.-E. Svensson, Coated stainless steel 441 as interconnect material for solid oxide fuel cells: oxidation performance and chromium evaporation, J. Power Sources 248 (2014) 1007–1013, http://dx.doi.org/10.1016/j.jpowsour.2013.08.089.
[14] A. Magrasó, H. Falk-Windisch, J. Froitzheim, J.-E. Svensson, R. Haugsrud, Reduced long term electrical resistance in Ce/Co-coated ferritic stainless steel for solid oxide fuel cell metallic interconnects, Int. J. Hydrogen Energy (2015), http://dx.doi.org/10.1016/j.ijhydene.2015.04.147.
[15] W.N. Liu, X. Sun, E. Stephens, M.A. Khaleel, Life prediction of coated and uncoated metallic interconnect for solid oxide fuel cell applications, J. Power Sources 189 (2009) 1044–1050, http://dx.doi.org/10.1016/j.jpowsour.2008.12.143.
[16] S.P. Jiang, X. Chen, Chromium deposition and poisoning of cathodes of solid oxide fuel cells—a review, Int. J. Hydrogen Energy 39 (2014) 505–531, http://dx.doi.org/10.1016/j.ijhydene.2013.10.042.
[17] C. Key, J. Eziashi, J. Froitzheim, R. Amendola, R. Smith, P. Gannon, Methods to quantify reactive chromium vaporization from solid oxide fuel cell interconnects, J. Electrochem. Soc. 161 (2014) C373–C381, http://dx.doi.org/10.1149/2.0041409jes.
[18] I. Belogolovsky, P.Y. Hou, C.P. Jacobson, S.J. Visco, Chromia scale adhesion on 430 stainless steel: effect of different surface treatments, J. Power Sources 182 (2008) 259–264, http://dx.doi.org/10.1016/j.jpowsour.2008.03.080.
[19] M. Sattari, R. Sachitanand, J. Froitzheim, J.E. Svensson, T. Jonsson, The effect of Ce on the high temperature oxidation properties of a Fe–22% Cr steel: microstructural investigation and EELS analysis, Mater. High Temp. 32 (2015) 118–122, http://dx.doi.org/10.1179/0960340914Z.00000000084.
[20] J.W. Fergus, Metallic interconnects for solid oxide fuel cells, Mater. Sci. Eng. A 397 (2005) 271–283, http://dx.doi.org/10.1016/j.msea.2005.02.047.
[21] M. Palcut, L. Mikkelsen, K. Neufeld, M. Chen, R. Knibbe, P.V. Hendriksen, Corrosion stability of ferritic stainless steels for solid oxide electrolyser cell interconnects, Corros. Sci. 52 (2010) 3309–3320, http://dx.doi.org/10.1016/j.corsci.2010.06.006.
[22] M.R. Ardigo, V. Parry, I. Popa, S. Chevalier, W. Chandra-Ambhorn, P. Phakpeetinan, Y. Wouters, Optimisation of metallic interconnects for hydrogen production by high temperature water vapour electrolysis, Defect Diffus. Forum 323–325 (2012) 239–244, http://dx.doi.org/10.4028/www.scientific.net/DDF.323-325.239.
[23] S. Guillou, C. Desgranges, S. Chevalier, Study of the growth mechanism of some oxide scales on Alloy 230 in high temperature vapor electrolysis (HTVE) conditions, Defect Diffus. Forum 323–325 (2012) 577–582, http://dx.doi.org/10.4028/www.scientific.net/DDF.323-325.577.
[24] H. Kurokawa, Oxidation behavior of Fe–16Cr alloy interconnect for SOFC under hydrogen potential gradient, Solid State Ionics 168 (2004) 13–21, http://dx.doi.org/10.1016/j.ssi.2004.02.008.

[25] E. Essuman, G.H. Meier, J. Żurek, M. Hänsel, W.J. Quadakkers, The effect of water vapor on selective oxidation of Fe–Cr alloys, Oxid. Met. 69 (2008) 143–162, http://dx.doi.org/10.1007/s11085-007-9090-x.
[26] S.R.J. Saunders, M. Monteiro, F. Rizzo, The oxidation behaviour of metals and alloys at high temperatures in atmospheres containing water vapour: a review, Prog. Mater. Sci. 53 (2008) 775–837, http://dx.doi.org/10.1016/j.pmatsci.2007.11.001.
[27] A. Srisrual, J.-P. Petit, Y. Wouters, A. Galerie, Multiscale photoelectrochemical studies on oxidized duplex stainless steels, Oxid. Met. 79 (2013) 337–347, http://dx.doi.org/10.1007/s11085-013-9357-3.
[28] R. Sachitanand, J.-E. Svensson, J. Froitzheim, The influence of Cr evaporation on long term Cr depletion rates in ferritic stainless steels, Oxid. Met. (2015), http://dx.doi.org/10.1007/s11085-015-9552-5.
[29] B. Tveten, G. Hultquist, T. Norby, Hydrogen in chromium: influence on the high-temperature oxidation kinetics in O_2, oxide-Growth mechanisms, and scale adherence, Oxid. Met. 51 (2016) 221–233, http://dx.doi.org/10.1023/A:1018866505708 (n.d.).
[30] S.H. Chan, H.K. Ho, Y. Tian, Modelling of simple hybrid solid oxide fuel cell and gas turbine power plant, J. Power Sources 109 (2002) 111–120, http://dx.doi.org/10.1016/S0378-7753(02)00051-4.
[31] S.H. Jensen, X. Sun, S.D. Ebbesen, R. Knibbe, M. Mogensen, Hydrogen and synthetic fuel production using pressurized solid oxide electrolysis cells, Int. J. Hydrogen Energy 35 (2010) 9544–9549, http://dx.doi.org/10.1016/j.ijhydene.2010.06.065.
[32] X. Sun, M. Chen, S.H. Jensen, S.D. Ebbesen, C. Graves, M. Mogensen, Thermodynamic analysis of synthetic hydrocarbon fuel production in pressurized solid oxide electrolysis cells, Int. J. Hydrogen Energy 37 (2012) 17101–17110, http://dx.doi.org/10.1016/j.ijhydene.2012.08.125.
[33] J. Froitzheim, H. Ravash, E. Larsson, L.G. Johansson, J.E. Svensson, Investigation of chromium volatilization from FeCr interconnects by a denuder technique, J. Electrochem. Soc. 157 (2010) B1295, http://dx.doi.org/10.1149/1.3462987.
[34] P. Kofstad, High Temperature Corrosion, Elsevier Applied Science Publishers Ltd., New York, 1988.
[35] J. Froitzheim, G.H. Meier, L. Niewolak, P.J. Ennis, H. Hattendorf, L. Singheiser, W.J. Quadakkers, Development of high strength ferritic steel for interconnect application in SOFCs, J. Power Sources 178 (2008) 163–173, http://dx.doi.org/10.1016/j.jpowsour.2007.12.028.
[36] J.E. Hammer, S.J. Laney, R.W. Jackson, K. Coyne, F.S. Pettit, G.H. Meier, The oxidation of ferritic stainless steels in simulated solid-oxide fuel-cell atmospheres, Oxid. Met. 67 (2007) 1–38, http://dx.doi.org/10.1007/s11085-006-9041-y.
[37] M. Stanislowski, J. Froitzheim, L. Niewolak, W.J. Quadakkers, K. Hilpert, T. Markus, L. Singheiser, Reduction of chromium vaporization from SOFC interconnectors by highly effective coatings, J. Power Sources 164 (2007) 578–589, http://dx.doi.org/10.1016/j.jpowsour.2006.08.013.
[38] B. Kuhn, C.A. Jimenez, L. Niewolak, T. Hüttel, T. Beck, H. Hattendorf, L. Singheiser, W.J. Quadakkers, Effect of laves phase strengthening on the mechanical properties of high Cr ferritic steels for solid oxide fuel cell interconnect application, Mater. Sci. Eng. A 528 (2011) 5888–5899, http://dx.doi.org/10.1016/j.msea.2011.03.112.
[39] K. Yamamoto, Y. Kimura, F.-G. Wei, Y. Mishima, Design of Laves phase strengthened ferritic heat resisting steels in the Fe–Cr–Nb(–Ni) system, Mater. Sci. Eng. A 329–331 (2002) 249–254, http://dx.doi.org/10.1016/S0921-5093(01)01586-6.
[40] R. Sachitanand, M. Sattari, J.-E. Svensson, J. Froitzheim, Evaluation of the oxidation and Cr evaporation properties of selected FeCr alloys used as SOFC interconnects, Int. J. Hydrogen Energy 38 (2013) 15328–15334, http://dx.doi.org/10.1016/j.ijhydene.2013.09.044.
[41] H. Falk-Windisch, J.E. Svensson, J. Froitzheim, The effect of temperature on chromium vaporization and oxide scale growth on interconnect steels for solid oxide fuel cells, J. Power Sources 287 (2015) 25–35, http://dx.doi.org/10.1016/j.jpowsour.2015.04.040.
[42] N. Birks, G.H. Meier, F.S. Pettit, Introduction to the High Temperature Oxidation of Metals, Second edition, Cambridge University Press, New York, 2006.
[43] J.A. Crawford, R.W. Vest, Electrical conductivity of single-crystal Cr_2O_3, J. Appl. Phys. 35 (1964) 2413, http://dx.doi.org/10.1063/1.1702871.
[44] D.B. Meadowcroft, F.G. Hicks, Electrical conduction processes and defect structure of chromic oxide, Proc. Br. Ceram. Soc. 23 (1972) 33–41.
[45] E.W.A. Young, J.H. Gerretsen, The oxygen patrial pressure dependence of the defect structure of chromium(III) oxide, J. Electrochem. Soc. 134 (1987) 2257–2260, http://dx.doi.org/10.1149/1.2100862.
[46] A. Holt, P. Kofstad, Electrical conductivity and defect structure of Cr_2O_3. I. High temperatures (> ~ 1000 °C), Solid State Ionics 69 (1994) 127–136, http://dx.doi.org/10.1016/0167-2738(94)90401-4.
[47] A. Holt, P. Kofstad, Electrical conductivity and defect structure of Cr_2O_3 II. Reduced temperatures (< ~ 1000 °C), Solid State Ionics 69 (1994) 137–143, http://dx.doi.org/10.1016/0167-2738(94)90402-2.
[48] N. Birks, G.H. Meier, F.S. Pettit, Mechanisms of oxidation, in: Introduction to High Temperature Oxidation Metals, second edition, Cambridge University Press, New York, 2006, pp. 39–74.
[49] W.C. Hagel, A.U. Seybolt, Cation diffusion in Cr_2O_3, J. Electrochem. Soc. 108 (1961) 1146–1152, http://dx.doi.org/10.1149/1.2427973.
[50] H. Hindam, D.P. Whittle, Microstructure, adhesion and growth kinetics of protective scales on metals and alloys, Oxid. Met. 18 (1982) 245–284, http://dx.doi.org/10.1007/BF00656571.
[51] E.A. Polman, T. Fransen, P.J. Gellings, The reactive element effect; ionic processes of grain-boundary segregation and diffusion in chromium oxide scales, J. Phys. Condens. Matter 1 (1989) 4497–4510, http://dx.doi.org/10.1088/0953-8984/1/28/001.
[52] R.E. Lobnig, H.P. Schmidt, K. Hennesen, H.J. Grabke, Diffusion of cations in chromia layers grown on iron-base alloys, Oxid. Met. 37 (1992) 81–93, http://dx.doi.org/10.1007/BF00665632.
[53] D. Caplan, G.I. Sproule, Effect of oxide grain structure on the high-temperature oxidation of Cr, Oxid. Met. 9 (1975) 459–472, http://dx.doi.org/10.1007/BF00611694.
[54] K.P. Lillerud, On high temperature oxidation of chromium, J. Electrochem. Soc. 127 (1980) 2397, http://dx.doi.org/10.1149/1.2129478.
[55] E.A. Polman, T. Fransen, P.J. Gellings, Oxidation kinetics of chromium and morphological phenomena, Oxid. Met. 32 (1989) 433–447, http://dx.doi.org/10.1007/BF00665448.
[56] P. Kofstad, K.P. Lillerud, On high temperature oxidation of chromium: II. Properties of Cr_2O_3 and oxidation mechanism of chromium, J. Electrochem. Soc. 127 (1980) 2410, http://dx.doi.org/10.1149/1.2129481.
[57] K.P. Lillerud, On high temperature oxidation of chromium: I. Oxidation of annealed, thermally ethced chromium at 800 °C–1100 °C, J. Electrochem. Soc. 127 (1980) 2397, http://dx.doi.org/10.1149/1.2129478.
[58] T. Brylewski, Application of Fe–16Cr ferritic alloy to interconnector for a solid oxide fuel cell, Solid State Ionics 143 (2001) 131–150, http://dx.doi.org/10.1016/S0167-2738(01)00863-3.
[59] M. Halvarsson, J.E. Tang, H. Asteman, J.-E. Svensson, L.-G. Johansson, Microstructural investigation of the breakdown of the protective oxide scale on a 304 steel in the presence of oxygen and water vapour at 600 °C, Corros. Sci. 48 (2006) 2014–2035, http://dx.doi.org/10.1016/j.corsci.2005.08.012.
[60] S. Canovic, J. Froitzheim, R. Sachitanand, M. Nikumaa, M. Halvarsson, L.-G. Johansson, J.-E. Svensson, Oxidation of Co- and Ce-nanocoated FeCr steels: a microstructural investigation, Surf. Coat. Technol. 215 (2013) 62–74, http://dx.doi.org/10.1016/j.surfcoat.2012.08.096.
[61] P.Y. Hou, J. Stringer, The effect of reactive element additions on the selective oxidation, growth and adhesion of chromia scales, Mater. Sci. Eng. A 202 (1995) 1–10, http://dx.doi.org/10.1016/0921-5093(95)09798-8.
[62] Z. Yang, G.-G. Xia, C.-M. Wang, Z. Nie, J. Templeton, J.W. Stevenson, P. Singh, Investigation of iron–chromium–niobium–titanium ferritic stainless steel for solid oxide fuel cell interconnect applications, J. Power Sources 183 (2008) 660–667, http://dx.doi.org/10.1016/j.jpowsour.2008.05.037.
[63] C.W. Bale, E. Bélisle, P. Chartrand, S.A. Decterov, G. Eriksson, K. Hack, I.-H. Jung, Y.-B. Kang, J. Melançon, A.D. Pelton, C. Robelin, S. Petersen, Factsage thermochemical software and databases—recent developments, Calphad 33 (2009) 295–311, http://dx.doi.org/10.1016/j.calphad.2008.09.009.
[64] E. Essuman, G.H. Meier, J. Zurek, M. Hänsel, L. Singheiser, T. Norby, W.J. Quadakkers, Effect of oxygen partial pressure on the oxidation behaviour of an yttria dispersion strengthened NiCr-base alloy, J. Mater. Sci. 43 (2008) 5591–5598, http://dx.doi.org/10.1007/s10853-008-2795-7.
[65] L. Niewolak, D.J. Young, H. Hattendorf, L. Singheiser, W.J. Quadakkers, Mechanisms of oxide scale formation on ferritic interconnect steel in simulated low and high pO_2 service environments of solid oxide fuel cells, Oxid. Met. 82 (2014) 123–143, http://dx.doi.org/10.1007/s11085-014-9481-8.
[66] S. Cruchley, H.E. Evans, M.P. Taylor, M.C. Hardy, S. Stekovic, Chromia layer growth on a Ni-based superalloy: sub-parabolic kinetics and the role of titanium, Corros. Sci. 75 (2013) 58–66, http://dx.doi.org/10.1016/j.corsci.2013.05.016.
[67] C. Issartel, H. Buscail, E. Caudron, R. Cueff, F. Riffard, S. El Messki, N. Karimi, L. Antoni, Effects of titanium on a ferritic steel oxidation at 950 °C, Mater. Sci. Forum 461–464 (2004) 69–76, 461-464.69 (accessed 20.06.15). http://www.scientific.net/MSF.
[68] E.J. Opila, D.L. Myers, N.S. Jacobson, I.M.B. Nielsen, D.F. Johnson, J.K. Olminsky, M.D. Allendor, Theoretical and experimental investigation of the thermochemistry of CrO_2OH_2(g), J. Phys. Chem. A 111 (2007) 1971–1980, http://dx.doi.org/10.1021/jp0647380.
[69] B.B. Ebbinghaus, Thermodynamics of gas phase chromium species: the chromium oxides, the chromium oxyhydroxides, and volatility calculations in waste incineration processes, Combust. Flame 93 (1993) 119–137, http://dx.doi.org/10.1016/0010-2180(93)90087-J.
[70] M.S. Sohal, J.E. O'Brien, C.M. Stoots, V.I. Sharma, B. Yildiz, A. Virkar, Degradation issues in solid oxide cells during high temperature electrolysis, J. Fuel Cell Sci. Technol. 9 (2012) 01107, http://dx.doi.org/10.1115/1.4003787.
[71] M.C. Tucker, H. Kurokawa, C.P. Jacobson, L.C. De Jonghe, S.J. Visco, A fundamental study of chromium deposition on solid oxide fuel cell cathode materials, J. Power Sources 160 (2006) 130–138, http://dx.doi.org/10.1016/j.jpowsour.2006.02.017.
[72] J.I. Gazzarri, O. Kesler, Short-stack modeling of degradation in solid oxide fuel cells, J. Power Sources 176 (2008) 138–154, http://dx.doi.org/10.1016/j.jpowsour.2007.10.047.